



Phase diagram of ferroelectrics with tricritical and Lifshitz points at coupling between polar and antipolar fluctuations

V. Liubachko,^{1,2} A. Oleaga,² A. Salazar,² R. Yevych¹,,¹ A. Kohutych¹,,¹ and Yu. Vysochanskii^{1,*}
¹*Institute for Solid State Physics and Chemistry, Uzhhorod University, Pidgirna Str. 46, Uzhhorod, 88000, Ukraine*
²*Departamento de Fisica Aplicada I, Escuela de Ingenieria de Bilbao, Universidad del Pais Vasco UPV/EHU, Plaza Torres Quevedo 1, 48013, Bilbao, Spain*



(Received 1 January 2020; revised manuscript received 24 May 2020; accepted 2 June 2020; published 15 June 2020)

Available experimental data about static and dynamic critical behaviors of $\text{Sn}_2\text{P}_2\text{S}_6$ -type ferroelectrics and $(\text{Pb}_y\text{Sn}_{1-y})_2\text{P}_2(\text{Se}_x\text{S}_{1-x})_6$ mixed crystals with a line of tricritical points and a line of Lifshitz points on the $T - x - y$ phase diagram, which meet at the tricritical Lifshitz point, are described in a combined Blume-Capel anisotropic next-nearest-neighbor Ising model. Such spin-1 Ising models with anisotropic competing first- and second-neighbor interactions is applied for the considered ferroelectrics with mixed displacive versus order/disorder character of phase transitions within the framework of a microscopic model with three-well total energy surface for ferroelectric distortion that was earlier built in an *ab initio* effective Hamiltonian approach. It was found that below the temperature of the tricritical Lifshitz point, the “chaotic” state accompanied by the coexistence of ferroelectric, metastable paraelectric, and modulated phases is expected. In addition to the frustration of polar fluctuations near the Brillouin zone center, in $\text{Sn}_2\text{P}_2\text{S}_6$ crystals the antipolar fluctuations also strongly develop in the paraelectric phase on cooling to the continuous phase-transition temperature T_0 . Here, the critical behavior can be described as a crossover between Ising and XY universality classes, which is expected near bicritical points with coupled polar and antipolar order parameters and competing instabilities in q space.

DOI: [10.1103/PhysRevB.101.224110](https://doi.org/10.1103/PhysRevB.101.224110)

I. INTRODUCTION

Competing order parameters produce rich phase diagrams of crystals with dipolar ordering in terms of temperature versus external fields, pressure, and doping [1]. In addition, the existence of competing ferroelectric, incommensurately modulated, and antiferroelectric states with different symmetries in the ground state of the system can be observed. The usual approach to describe the phase diagrams is the Landau-Ginzburg expansion of the free-energy density in terms of the order parameters [2]. At microscopic level, the phase diagrams can be obtained by using mean-field approximations of simplified model Hamiltonians [3]. In any case, the system symmetry determines the main qualitative properties of the phase diagram.

The active role of several types of mode-mode couplings is also reflected in the complex shape of the local potential for the crystal lattice ferroelectric distortion. It determines the appearance of phase diagrams with different multicritical points that have been extensively studied experimentally and within the framework of phenomenological models for the case of oxide materials [4–7]. A variety of nonpolar antiferrodistortive, ferroelectric, and antiferroelectric phase transitions in perovskite compounds show their sensitivity to chemical composition, structural defects, and pressure, which arises from a delicate balance of interatomic couplings. To

describe the structural transitions accurately, the total-energy techniques, which incorporate the effects of charge distortion and covalency, were developed [8]. The first-principles calculations within the framework of density-functional theory provide considerable insight into the nature of the total energy surface in crystals. For ferroelectric compounds, the polarization generated by various lattice distortions can be studied directly, using an effective Hamiltonian based on a Taylor expansion of the energy surface around the paraelectric phase structure, including soft optical modes and strain components as the possible distortions [9,10]. This approach has been applied to investigations of the zone-center phonons in ferroelectrics or antiferrodistortive and antiferroelectric degrees of freedom [11–13]. The study of the effective Hamiltonian by Monte Carlo simulations allows us to investigate the phase transitions at finite temperature [9–13].

Because of the simple crystal structure of the oxide perovskites, the first-principles scheme based on the local-mode approach has been successfully applied to study their phase transitions. For chalcogenide ferroelectrics of the $\text{Sn}_2\text{P}_2\text{S}_6$ family, the strongly pronounced nonlinear phenomena are related to the much higher polarizability (compared to oxides) of the anion sublattice. Together with a lower symmetry of the crystal lattice, this determines a more complex nature of the phase transitions and a rich set of scenarios for critical behavior realization [14–17].

Ferroelectrics of the $\text{Sn}_2\text{P}_2\text{S}_6$ family are promising candidates for applications in red and near-infrared spectral diapason photorefractive [18] and photovoltaics [19]

*vysochanskii@gmail.com

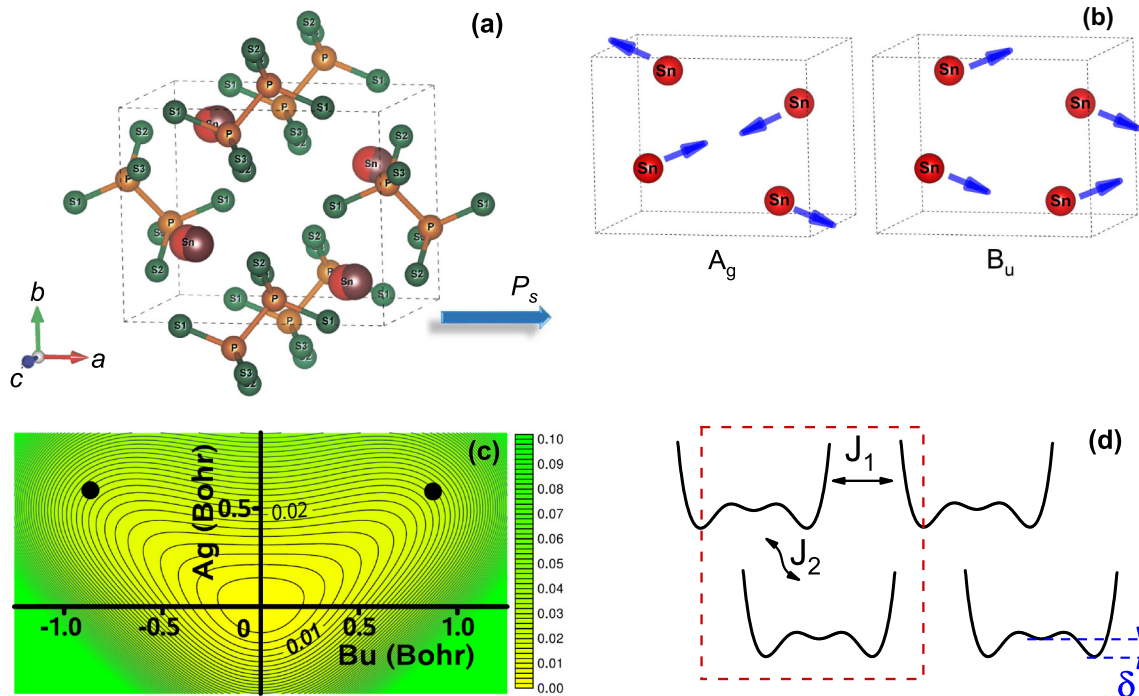


FIG. 1. (a) The crystal structure of $P2_1/n$ paraelectric phase of $\text{Sn}_2\text{P}_2\text{S}_6$ crystals [27]. The crystallographic b axis coincides with the 2_1 symmetry axis and the (010) plane with the glide plane n . The inversion center is placed in the middle of the $P - P$ bonds of $(\text{P}_2\text{S}_6)^{4-}$ anions. The positions of the tin cations (large spheres) in the paraelectric and ferroelectric phases are shown by different colors. Two sublattices are presented by two formula units in a monoclinic elementary cell. (b) Schematic representation (for tin ions only) of eigenvectors of the lowest energy polar B_u (39 cm^{-1}) and the fully symmetrical A_g (41 cm^{-1}) long wave modes [28]. (c) Frozen-phonon energy surface (in eV) for a linear combination of A_g and B_u mode amplitudes for $\text{Sn}_2\text{P}_2\text{S}_6$ within LDA calculations [28]. Black circles denote the positions of the global ferroelectric minima. (d) Presentation of the BC-ANNI model which describes an array of pseudospins related to $\text{Sn}_2\text{P}_2\text{S}_6$ formula units in two sublattices and flipped in the three-well potential with crystal field strength δ (energy difference between central and side wells). J_1 —NN interaction within sublattices, J_2 —NNN interaction between sublattices.

for energy storage [20] and low-temperature thermometry [21,22], as well as for the development of multilevel-cell-type memory technology [23]. The possibilities of ultrafast spontaneous polarization switching [24] and peculiarities in the ferroelectric ordering and domain structure morphology at nanoscale [25,26] are also important for new technologies based on ferroics with linear and nonlinear coupling between unstable lattice polar modes and antipolar or antiferrodistorsive degrees of freedom.

In $\text{Sn}_2\text{P}_2\text{S}_6$ crystals, the second order phase transition at $T_0 \approx 337 \text{ K}$ with lattice symmetry lowering from $P2_1/n$ to Pn [see Fig. 1(a)] has mixed displacive-order/disorder character [29,30], which is manifested by the high values of both the transition entropy [31] $\Delta S = 8.6 \text{ JK}^{-1}\text{mol}^{-1}$ and the dielectric anomaly of the Curie-Weiss constant [32] $C \approx 10^5 \text{ K}$. In $\text{Sn}_2\text{P}_2\text{S}_6$ crystals under compression, the second-order transition line $T_0(p)$ monotonously decreases and, after reaching the tricritical point (TCP) at $p_{\text{TCP}} \approx 0.6 \text{ GPa}$ and $T_{\text{TCP}} \approx 220 \text{ K}$, it becomes first order [33,34]. At Sn by Pb replacement in $(\text{Pb}_y\text{Sn}_{1-y})_2\text{P}_2\text{S}_6$ solid solutions, the continuous phase transitions line $T_0(y)$ become first order at $y \geq y_{\text{TCP}} \approx 0.2$ and $T \leq T_{\text{TCP}} \approx 220 \text{ K}$, and the paraelectric phase becomes stable when cooling down to 0 K for $y \geq 0.6$ [35,36]. At sulfur by selenium substitution in $\text{Sn}_2\text{P}_2(\text{Se}_x\text{S}_{1-x})_6$ mixed crystals, the incommensurate (IC) phase appears for $x \geq$

$x_{\text{LP}} \approx 0.28$ [where x_{LP} is the concentration of the Lifshitz point (LP)] on the temperature-concentration diagram [17]. The virtual paraelectric-ferroelectric transition (inside the IC phase) becomes first order at $x \geq x_{\text{VTCP}} \approx 0.6$ and $T \leq T_{\text{VTCP}} \approx 220 \text{ K}$ [16].

It is seen that under any influence that lowers the ferroelectric phase transition temperature below 220 K , the character of the transition evolves to first order, which has been explained within a model with three-well total energy surface for ferroelectric distortion. [28,35,37].

A completely *ab initio* effective Hamiltonian approach has been used to theoretically study the continuous ferroelectric phase transition in $\text{Sn}_2\text{P}_2\text{S}_6$ crystals [28]. The paraelectric structure distortions were decomposed in terms of amplitudes of the Brillouin zone center A_g and B_u optic modes. It was found that the lowest energy A_g and B_u modes make the largest ferroelectric distortions, but the contributions of the other higher energy modes can't be neglected either. The eigenvector of the low-energy optical B_u mode describes the in-phase displacements of the four Sn^{2+} cations mainly along the direction of the lattice spontaneous polarization and the corresponding counterphase displacements of the two anion complexes $(\text{P}_2\text{S}_6)^{4-}$. In the low-energy nonpolar A_g vibration, only the out-of-phase displacements in the cation sublattice are observed [see Fig. 1(b)].

The frozen-phonon calculations of the total energy for the low-energy B_u mode do not point to any additional minima, which might be related to the ferroelectric instability. But studying the potential energy surface in the subspace of low-energy A_g and B_u modes, a strong deviation from harmonic behavior can be clearly seen, though the global ferroelectric minima were not observed yet. The energy positions of the ferroelectric global minima can be reached only in the subspace of all 15 A_g and 13 B_u normal coordinates and four monoclinic components of strain [28].

The order parameter of the phase transition in the crystal is determined as a valley line in the 32-dimensional phase space. The obtained energy profile has a three-well shape [28], where two ferroelectric valleys arise from the nonequivalent lattice distortions $A_g \pm B_u$ because of the strong nonlinear $A_g B_u^2$ interaction [see Fig. 1(c)].

As a local polar distortion, the set of the linear atomic displacements which account for all A_g and B_u modes was chosen. A pseudospin form of the effective Hamiltonian [9,10,28] has been built up with five parts: (i) a local-mode self-energy, (ii) a long-range dipole-dipole interaction, (iii) a short-range interaction between local soft modes, (iv) an elastic energy, and (v) an interaction between the local modes and local strain. The resulting Hamiltonian was studied using Monte Carlo simulations [28]. The temperature evolution of the pseudospin distribution in a three-well local potential was found and it is comparable with experimental data of ^{31}P NMR spectroscopy [38].

The nonlinear mode interaction, which leads to the three-well shape of the potential energy surface, is a result of a significant electron-phonon interaction that, in the case of $\text{Sn}_2\text{P}_2\text{S}_6$ ferroelectrics, can be described on the basis of a second-order Jahn-Teller effect related to the stereoactivity of electrons lone pair of Sn^{2+} cations [28,39]. The charge disproportionation of phosphorous cations $P^{4+} + P^{4+} \leftrightarrow P^{3+} + P^{5+}$ also originates an electronic contribution to the local ferroelectric distortions that are taken as pseudospins [28,37,39].

The phase transition in $\text{Sn}_2\text{P}_2\text{S}_6$ crystals with mixed displacive-order/disorder character was analyzed [37] within the framework of the three-state Blume-Capel (BC) model [40,41] that supposes 0, +1, and -1 values for local pseudospins. It should be noted that the BC model follows from the Blume-Emery-Griffiths (BEG) model [42,43] at zero biquadratic spin interaction. This model has two order parameters (dipolar and quadrupolar) that can be related to B_u and A_g modes in the case of $\text{Sn}_2\text{P}_2\text{S}_6$ ferroelectrics. The BEG model predicts the TCP presence on a temperature-pressure or temperature-composition phase diagram of $(\text{Pb}_y\text{Sn}_{1-y})_2\text{P}_2\text{S}_6$ mixed crystals. The TCP presence and the lowering of the phase-transition temperature to 0 K are determined by pressure or composition evolution of the local three-well potential shape (change of the energy difference δ between central and side wells [see Fig. 1(d)]).

The appearance of the IC phase in the $\text{Sn}_2\text{P}_2\text{S}_6$ family of crystals has already been explained [32] by using the discrete axial Ising model—anisotropic next-nearest-neighbor Ising (ANNNI) model [44]—which takes into consideration two sublattices of $\text{Sn}_2\text{P}_2\text{S}_6$ -type crystal structure with two formula units in the elementary cell [see Fig. 1(d)]. This model considers short-range interaction $J_1 > 0$ between the nearest

neighbors (NNs) and interaction $J_2 < 0$ between next-nearest neighbors (NNNs). The ratio of these interactions $\lambda = -J_2/J_1$ changes at sulfur by selenium substitution in $\text{Sn}_2\text{P}_2(\text{Se}_x\text{S}_{1-x})_6$ mixed crystals, the IC phase appears at the LP with coordinate $\lambda = 0.25$. It was estimated that λ changes from 0.23 for composition with $x = 0$ to 0.3 for $x = 1$ [32]. The wave vector of the transverse modulation wave of the described IC phase is oriented near the [001] direction in the (010) monoclinic symmetry plane [45]. The spontaneous polarization vector \vec{P}_s also lies in this symmetry plane and is oriented near the [100] direction [see Fig. 1(a)].

The neutron scattering data [45,46] demonstrate both displacive and order/disorder peculiarities of phase transitions in $\text{Sn}_2\text{P}_2\text{S}(\text{Se})_6$ crystals. The flexoelectric coupling between soft optical and acoustic phonon branches near the Brillouin zone center as their repulsion due to the same symmetry along q_z direction of reciprocal space is related to the displacive nature of paraelectric-ferroelectric and paraelectric-IC transitions. This coupling has also been observed in temperature anomalies of ultrasound and hypersound velocity [47]. In the continuous approximation, the linear interaction between optical and acoustic phonons is presented by the Lifshitz-like invariant $(dP_x/dz)u_{xz}$ in the thermodynamic potential [48,49]. Its growth at changing from $\text{Sn}_2\text{P}_2\text{S}_6$ to $\text{Sn}_2\text{P}_2\text{Se}_6$ is caused by a higher covalence of chemical bonds in a selenide compound [50].

The neutron scattering data [46] also show the presence of a flat lowest-energy transverse optical branch along the q_y direction in the paraelectric phase of $\text{Sn}_2\text{P}_2\text{S}_6$ crystals, which is a demonstration of the order/disorder nature of the phase transition. The presence of diffuse x-ray scattering along the q_y direction in the paraelectric phase near temperature T_0 [51] confirms the important role of the short-wave antipolar fluctuations for the lattice instability.

In this paper, we use the spin-1 Ising model with competing interactions [40,52] for the description of the phase diagram topology for ferroelectrics with TCPs and LPs, for example, of $\text{Sn}_2\text{P}_2\text{S}_6$ -based ferroelectric mixed crystals. To estimate the model parameters, we have used previously obtained experimental data and determined temperature-composition phase diagrams of $(\text{Pb}_y\text{Sn}_{1-y})_2\text{P}_2(\text{Se}_x\text{S}_{1-x})_6$ ferroelectrics. In addition, the available experimental data about the important role of the short-wave antipolar fluctuations in the complex nature of ferroelectric phase transitions for $\text{Sn}_2\text{P}_2\text{S}_6$ -type crystals are analyzed together with the consideration of their critical behavior peculiarities.

II. PHASE DIAGRAM WITH TRICRITICAL LIFSHITZ POINT

A spin-1 Ising model is introduced and solved in the mean-field approximation by BEG [42]. The total Hamiltonian of this BEG model,

$$H = -J \sum_{\langle ij \rangle} s_i s_j - K \sum_{\langle ij \rangle} s_i^2 s_j^2 + \delta \sum_i s_i^2, \quad (1)$$

includes only the NN interactions J , a biquadratic exchange of strength K , and a crystal field of strength δ . In Eq. (1), the spin $s_{ij} = 0, \pm 1$ is at each site i of a lattice and $\langle ij \rangle$ denotes summation over all the NN pairs of sites. The BEG model is

a basic model for systems in which the phase transitions can be driven by symmetry-breaking (dipolar) fluctuations ($s_i = \pm 1$) and by density (quadrupolar) fluctuations ($s_i^2 = 1, 0$). Changing the parameters of this BEG model produces many different types of phase diagrams, including TCPs and higher order multicritical points [42,43].

The simplest model used for investigations of modulated magnetic structures is the spin-1/2 ANNNI model [44]. This model contains the NN ferromagnetic interactions ($J_0 > 0$) in the xy plane, and the competing NN ferromagnetic ($J_1 = J_0 > 0$) and the NNN antiferromagnetic ($J_2 < 0$) interaction terms in the z direction. The ANNNI model describes a rich phase diagram with LP and transitions between uniform and modulated phases. The extension of such a model to the study of a spin-1 system with competing interactions including $s_{ij} = 0, \pm 1$ states was done by defining a simple cubic lattice spin-1 ANNNI model with the addition of a crystal field of strength δ and a biquadratic spin interaction term with strength K [52]. For the $s = 1$ lattice model, different phases are characterized by different values of the dipolar order parameter $P_i = \langle s_i \rangle$ and the quadrupolar order parameter $Q_i = \langle s_i^2 \rangle$. Here, in addition to the competition between dipolar interactions J_1 and J_2 that produces modulated phases, the competition between both dipolar (J_1, J_2) and quadrupolar (K) couplings induces the appearance of $s = 0$ states.

In the beginning [52], in the mean-field treatment, the phase diagram with a LP and a transition between uniform and modulated phases was obtained only for a particular value of J_1/K ratio. Further investigations have been performed [40] with special attention on including the influence of a crystal field strength δ to determine the position of the TCP on the phase diagram, as well as the competing interaction ratio $\lambda = -J_2/J_1$ to determine the presence of the LP. To do this, the biquadratic spin interaction K was neglected, and the simplified model becomes a BC model [40,41] with axial NNN interactions. Such a BC-ANNNI model has the following Hamiltonian:

$$H = -J_0 \sum_{(ij)}^{(xy)} s_i s_j - J_1 \sum_{(ij)}^{(z)} s_i s_j - J_2 \sum_{\langle\langle ij \rangle\rangle}^{(z)} s_i s_j + \delta \sum_i s_i^2. \quad (2)$$

Here again the NN interactions $J_1 = J_0 > 0$ and NNN interaction $J_2 < 0$. We applied this model to study the ferroelectric ordering in $\text{Sn}_2\text{P}_2\text{S}_6$ -type crystals. In our approximation, the local lattice distortions $A_g \pm B_u$ with a three-well shape of the energy profile [28] [see Fig. 1(c)] are taken as pseudospins that satisfy the BC model with the Hamiltonian Eq. (1) at $K = 0$. The pseudospins are related to $\text{Sn}_2\text{P}_2\text{S}_6$ formula units. The crystal lattice of $\text{Sn}_2\text{P}_2\text{S}_6$, containing two formula units in the elementary cell, can be presented as two sublattices of pseudospins, so the coupling between the nearest pseudospins from the same sublattice is the NN interaction J_1 , while the coupling of the nearest pseudospins from different sublattices is the NNN interaction J_2 [see Fig. 1(d)]. For the description of the ferroelectric ordering in the considered compound, we apply the spin-1 model with short-range competing interactions, assuming that long-range dipole-dipole and elastic interactions are encapsulated in the

local three-well potential for ferroelectric distortions that was established by first-principles LDA calculations [28].

The BC-ANNNI model [40] displays a multicritical behavior such as tricriticality as well as the possibility of the presence of a LP. The tricritical Lifshitz point (TCLP) is predicted at the meeting point of TCP and LP lines [53–55]. In this model (as for the original ANNNI model [44]), the relation between two interactions is written in the form $\lambda = -J_2/J_1$, where J_1 is the effective first neighbors' positive interaction and J_2 is the negative coupling of NNNs. The paraelectric-ferroelectric second-order transition line was found as [40]

$$\lambda = 1 - \frac{t}{1 + 0.5e^{\Delta/t}}, \quad (3)$$

and from the paraelectric phase into a modulated one through a continuous transitions line:

$$\lambda = \frac{t}{1 + 0.5e^{\Delta/t}}. \quad (4)$$

Here $t = T/J_1$, and $\Delta = \delta/J_1$. The parameter δ is related to the single-ion term [37,42]. At $\lambda = 0.25$, the paraelectric borders obtained from Eqs. (3) and (4) meet at a LP. Considering the above-mentioned conditions, the line of LPs was found by means of the following equation:

$$\Delta = t_{\text{LP}} \ln \frac{1 - 2t_{\text{LP}}}{t_{\text{LP}}}. \quad (5)$$

After reaching a value $\Delta \approx 0.231$, the paraelectric borders begin to split and there is no LP anymore. Near this Δ value, the LP line coincides with the TCP line and the end point line [40]. The calculated $t - \lambda - \Delta$ phase diagram is depicted in Fig. 2.

To build the $T - \lambda - \Delta$ phase diagram for ferroelectrics in the system $\text{Sn}(\text{Pb})_2\text{P}_2\text{S}(\text{Se})_6$, we have compared the above-described theoretical phase diagram with the experimentally determined temperature-concentration phase diagram for $(\text{Pb}_y\text{Sn}_{1-y})_2\text{P}_2(\text{Se}_x\text{S}_{1-x})_6$ mixed crystals [32]. To do it, we need to translate it into $t - \lambda - \Delta$ coordinates. Here we suppose that the parameter Δ depends linearly only on composition y in the cation sublattice, and parameter λ varies linearly only with composition x of the anion sublattice. The experimentally observed [56] TCLP for $(\text{Pb}_{0.05}\text{Sn}_{0.95})_2\text{P}_2(\text{Se}_{0.28}\text{S}_{0.72})_6$ at $T_{\text{TCLP}} \approx 259$ K in $t - \lambda - \Delta$ coordinates will correspond to the next position: $t = 0.158249$, $\lambda = 0.5$, $\Delta = 0.23105$. The LP with the composition $\text{Sn}_2\text{P}_2(\text{Se}_{0.28}\text{S}_{0.72})_6$ at temperature $T_{\text{LP}} \approx 284$ K (Ref. [17]) will lie on the line of LPs obtained from Eq. (5) at $t = 0.17345$, $\lambda = 0.5$, $\Delta = 0.22997$. For mixed $\text{Sn}_2\text{P}_2(\text{Se}_x\text{S}_{1-x})_6$ crystals in the framework of the ANNNI model, a linear variation of the λ parameter with composition x was assumed with the values 0.23, 0.25, and 0.30 for $\text{Sn}_2\text{P}_2\text{S}_6$, $\text{Sn}_2\text{P}_2(\text{Se}_{0.28}\text{S}_{0.72})_6$, and $\text{Sn}_2\text{P}_2\text{Se}_6$, respectively [32]. At the constant value $\Delta = 0.22997$, the coordinates for these concentrations on the $t - \lambda - \Delta$ diagram are the following: $t_0 = 0.20582$, $\lambda = 0.23$ for $\text{Sn}_2\text{P}_2\text{S}_6$ with $T_0 = 337$ K; $t_c = 0.13436$, $\lambda_c = 0.30$, and $t_i = 0.11799$, $\lambda_i = 0.30$ for $\text{Sn}_2\text{P}_2\text{Se}_6$ with $T_c = 220$ K, and $T_i = 193$ K [32].

When substituting tin by lead, the shape of the local three-well potential changes, and the coordinates of the TCP in the $(\text{Pb}_y\text{Sn}_{1-y})_2\text{P}_2\text{S}_6$ mixed crystals in the mean-field approximation on the BC model [57] can be determined of a linear

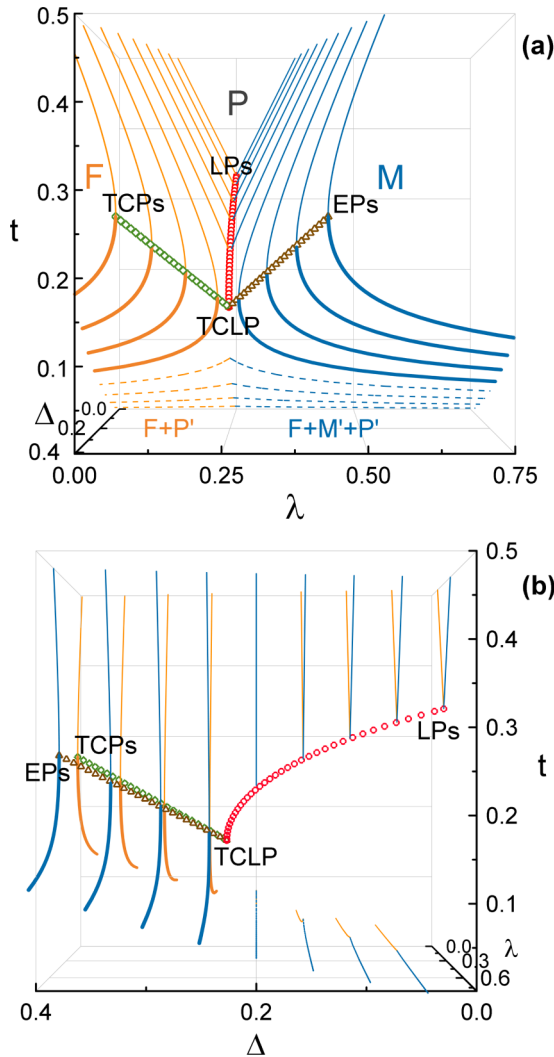


FIG. 2. (a) Front and (b) side views on calculated $t - \lambda - \Delta$ diagram. Solid lines show paraelectric-ferroelectric (orange) and paraelectric-modulated (blue) borders, Lifshitz point (LP) lines (red circles), tricritical point (TCP) lines (green squares), and end point (EP) lines (brown triangles). Thin lines indicate the second-order phase transitions while thick lines are the first-order ones. Letters F, P, and M correspond to ferroelectric, paraelectric, and modulated phases. The coexistence of ferroelectric and metastable paraelectric ($F + P'$) and ferroelectric, metastable paraelectric, and commensurate modulated phases ($F + M' + P'$) below the dashed lines are also shown.

variation of Δ with respect to y , and unchanged intercell interactions. According to the earlier performed analysis for $(\text{Pb}_y\text{Sn}_{1-y})_2\text{P}_2\text{S}_6$ mixed crystals,[37] the calculated $t - \Delta$ diagram (at $\lambda = 0.23$) is shown in Fig. 3. It was found that the TCP has coordinates $\lambda = 0.23, t = 0.13436, \Delta = 0.23577$.

As the intersite interaction, J_1 is an almost unchanged quantity [37]; we assume that, on increasing the lead concentration in $(\text{Pb}_y\text{Sn}_{1-y})_2\text{P}_2\text{Se}_6$ mixed crystals (with $\lambda = 0.3$), the value of Δ will change in the same way as in $(\text{Pb}_y\text{Sn}_{1-y})_2\text{P}_2\text{S}_6$ solid solutions. Accordingly, the experimental phase diagram in $t - \lambda - \Delta$ coordinates is presented in Fig. 4.

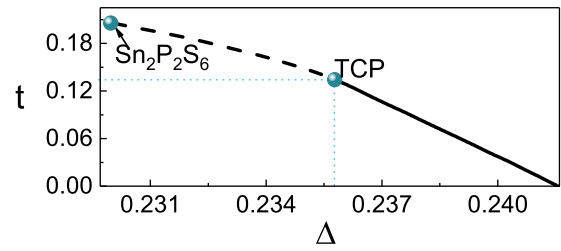


FIG. 3. Dependence of the phase transition temperature on the single-ion term in dimensionless $t - \Delta$ coordinates calculated in the mean-field approximation on the BC model [37,57]. Dashed and solid lines indicate second- and first-order transitions, respectively, that meet at the tricritical point.

From the calculated $t - \lambda - \Delta$ diagram, it follows that the LP line terminates at TCLP, and this multicritical point can be considered as a Lifshitz end point. The LP line in TCLP

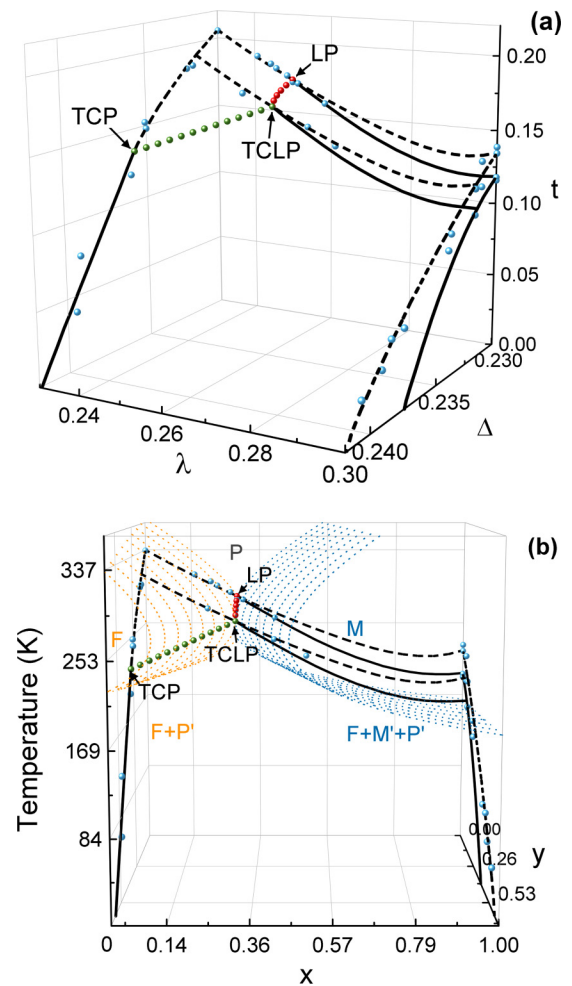


FIG. 4. (a) Experimental phase diagram in $t - \lambda - \Delta$ coordinates for $(\text{Pb}_y\text{Sn}_{1-y})_2\text{P}_2(\text{Se}_x\text{S}_{1-x})_6$ ferroelectrics and (b) front view of both experimental and calculated phase diagrams in temperature-concentration $T - x - y$ coordinates. Dashed and solid lines denote second-order and first-order phase transitions, respectively. Green and red spheres correspond to tricritical point lines and Lifshitz point lines, blue spheres to the calorimetric data [36,56,58–62].

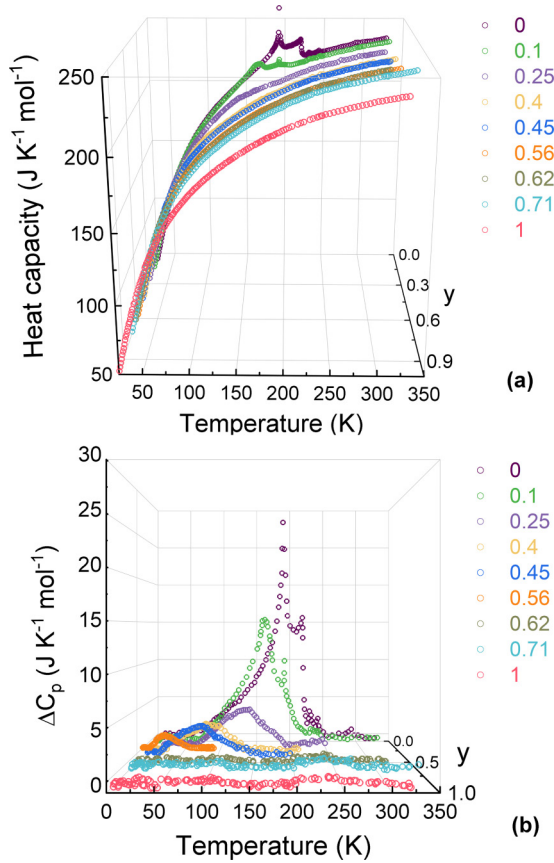


FIG. 5. Temperature dependence of (a) heat capacity according to experimental data [63] and (b) related to the phase transition excess heat capacity for $(\text{Pb}_y\text{Sn}_{1-y})_2\text{P}_2\text{Se}_6$ crystals.

splits into the TCP line and the end point line. When Δ is big enough, the paraelectric-modulated critical line ends at the end point [40].

As is well seen from Fig. 2, at a low enough value of the parameter Δ , the paraelectric-ferroelectric second-order transition line and the paraelectric-modulated continuous phase transitions line meet at the LP. For $\Delta > \Delta_{\text{TCP}} \approx 0.23$, the lines obtained from Eqs. (3) and (4) begin to be separated

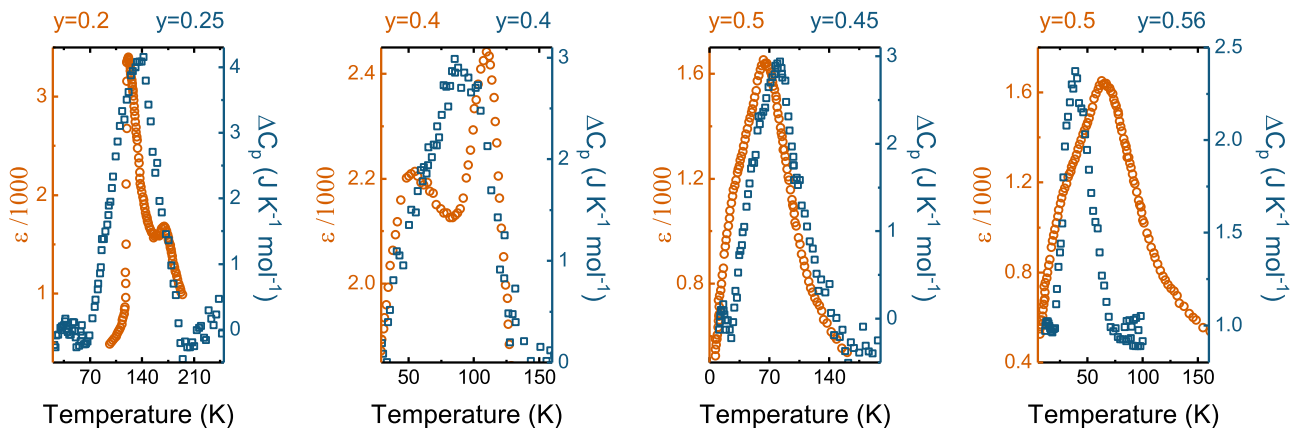


FIG. 6. Comparison of the anomalies for low-frequency dielectric susceptibility (according to data [21,22,64]) and excess heat capacity (according to data [63]) in the region of the phase transitions for $(\text{Pb}_y\text{Sn}_{1-y})_2\text{P}_2\text{Se}_6$ crystals.

by paraelectric region—the paraelectric phase can exist down to $T = 0$.

For high lead concentrations ($y > 0.2$), at low temperatures a chaotic state can be observed [40]. This state presents a mixture of paraelectric, ferroelectric, and modulated phases. Such peculiarity can be seen on the excess heat capacity ΔC_p and anomalous temperature dependencies of dielectric susceptibility ε' in $(\text{Pb}_y\text{Sn}_{1-y})_2\text{P}_2\text{Se}_6$ crystals, according to recent investigations [21,22,63,64]. For small lead concentrations, there are clear anomalies of $\Delta C_p(T)$ and $\varepsilon'(T)$ at paraelectric-IC (T_i) and IC-ferroelectric (T_c) phase transitions (see Figs. 5 and 6). However, for $y \geq 0.2$, the $\Delta C_p(T)$ and $\varepsilon'(T)$ anomalies in the vicinity of the lock-in transition (T_c) are strongly smeared and become similar to the observed anomalies in a case of relaxor ferroelectrics. Such chaoticization can be related to a synergy of frustration effects and nonlinearity of the system with the three-well local potential.

The ANNI model with two structural sublattices reflects the main properties of ferroelectrics that are related to the LP and IC phases on their phase diagram. Above, for the description of the presence of a TCP on the phase diagram of $\text{Sn}_2\text{P}_2\text{S}_6$ family ferroelectrics, the quadrupole-quadrupole coupling has been neglected and the BC model approximation was used [41]. A more accurate consideration of these ferroelectrics with two structural sublattices can be performed in the frame of BEG model [42,43]. This three-state model is based on two order parameters—dipolar and quadrupolar (B_u and A_g symmetry variables in the case of $\text{Sn}_2\text{P}_2\text{S}_6$) [28,39]. Therefore, in addition to dipole-dipole intersite coupling, the quadrupole-quadrupole interaction can also be important. In the case of two sublattices, taking into account the quadrupole-quadrupole interactions can complicate the topology of the temperature-composition phase diagram. On such a diagram, in addition to (or instead of) the presence of a TCP, other multicritical points can appear, such as a triple point, a critical end point, a bicritical point, and a tetracritical point [43]. In the case of negative quadrupole-quadrupole coupling while lowering the temperature, in addition to the ferroelectric state, ferroelectric and antiquadrupolar phases can also appear [43]. With the growth of positive quadrupole-quadrupole coupling, the TCP transforms into a triple point.

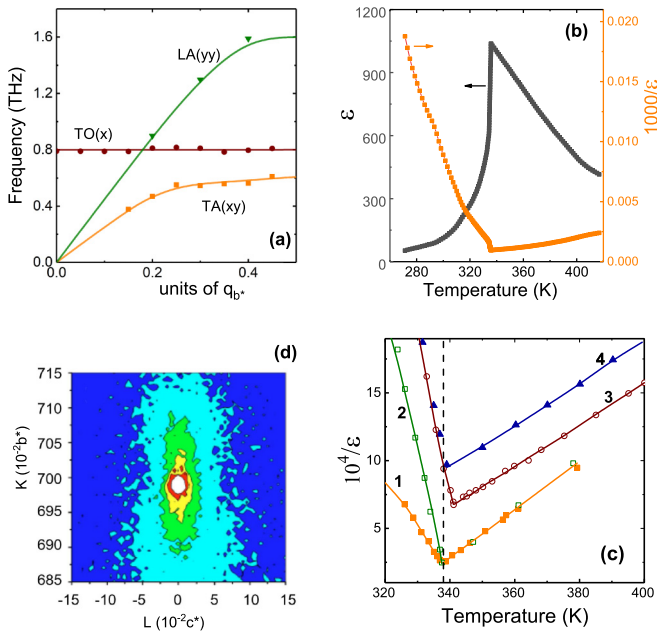


FIG. 7. (a) Determined by neutron scattering at 440 K transverse soft optical $TO(X)$, acoustic longitudinal $LA(XX)$ and transverse $TA(XY)$ phonon branches along q_y direction of $\text{Sn}_2\text{P}_2\text{S}_6$ crystal monoclinic Brillouin zone [46]; (b) temperature dependence of the dielectric susceptibility and its reciprocal from submillimeter soft optical mode contribution near the phase transition in $\text{Sn}_2\text{P}_2\text{S}_6$ crystal [68]; (c) comparison of the inverse of the dielectric susceptibility temperature dependence in $\text{Sn}_2\text{P}_2\text{S}_6$ crystal [69] for 20 MHz—1, 4 GHz—2, 27 GHz—3 and submillimeter soft optical mode contribution—4; (d) diffuse x-ray scattering at $T_0 + 2$ K in the paraelectric phase of $\text{Sn}_2\text{P}_2\text{S}_6$ crystal in the plane (OKL) of the Brillouin zone [51].

In such a case, on cooling in the paraelectric phase the first-order transition with change of quadrupolar order parameter occurs, and with further temperature lowering the second-order transition into a ferroelectric state is observed [43].

III. POLAR AND ANTIPOLAR FLUCTUATION COUPLING

The above-mentioned examples of possible complications of experimentally observed phase diagrams for objects with complex local potential for ferroelectric distortion demonstrate the proximity of the phase transitions to higher order multicritical points, like a tetracritical point, and give evidence of the importance of higher order invariants in the thermodynamic potential of the investigated ferroelectric crystals. Such possibility was earlier demonstrated [65–67] when the IC phase properties near lock-in transition into the ferroelectric phase in $\text{Sn}_2\text{P}_2\text{S}_6$ crystals were theoretically explained.

For $\text{Sn}_2\text{P}_2\text{S}_6$ ferroelectrics, the experimental data of neutron scattering, dielectric susceptibility, and hysteresis loop investigations present rich information about the complex character of the phase transitions. The neutron scattering data [46] show the presence of a flat lowest-energy transverse optical branch along q_y direction at $T = 440$ K in the paraelectric phase [see Fig. 7(a)]. This phonon branch is polarized near $[100]$ direction and softens at cooling. The polar soft

optical mode, according to the submillimeter spectroscopy data near 10^{12} Hz [68], contributes only $\Delta\varepsilon' = 1000$ to the dielectric susceptibility maximum near $T_0 \approx 337$ K [see Fig. 7(b)]. When the frequency is lowered down to 10^7 Hz, the dielectric susceptibility near T_0 rises to $10^4 - 10^5$ [see Fig. 7(c)] [69] and at lower frequency obeys the Curie-Weiss law $\varepsilon' = C(T - T_0)^{-1}$ with $C \approx 0.6 \times 10^5$ K.

On cooling in the paraelectric phase of a $\text{Sn}_2\text{P}_2\text{S}_6$ crystal, not only long wave polarization fluctuations are developed near the Brillouin zone center, which are proportional to the reciprocal of the polar soft optical mode (with B_u symmetry at $q \rightarrow 0$) frequency square. Near the Brillouin zone edge, at $q_y = \pi/b$, critical growth also occurs for fluctuations that are related to the eigenvector of short length phonons from the soft optical branch $B(q_y)$. The development of the aforementioned fluctuations was observed directly [see Fig. 7(d)] [51] by inelastic x-ray scattering at $T_0 + 2$ K.

As discussed above, the local three-well potential follows from a nonlinear interaction of polar B_u modes with fully symmetrical A_g modes (like $A_g B_u^2 + A_g^2 B_u^2$) at the Brillouin zone center [28,39]. But on the matter of the soft optical mode flatness in the q_y direction [46], the nonlinear phonon-phonon interaction can be realized with the involvement of phonons from different points of the Brillouin zone. In the simplest way, such a possibility can be described by a mean-field-solved model of quantum anharmonic oscillators [23,37,70,71] that is based on a three-well on-site potential involving first- and second-neighbor intersite interactions. Here we consider nonlocal interactions in the q_y direction (instead of the above considered frustration of J_1 and J_2 intersite interactions that are related to the IC phase appearance with modulation wave vector q_z). The phase diagram calculated with such a model contains a tetracritical point at which two second-order transition lines (from paraelectric into ferroelectric phase and between paraelectric and antipolar phases) intersect. It was found [23] that for $\text{Sn}_2\text{P}_2\text{S}_6$ crystals below T_0 , the coexistence of antipolar and ferroelectric phases can be presented.

The assumption that in $\text{Sn}_2\text{P}_2\text{S}_6$ crystals the phase transition at $T_0 \approx 337$ K is placed near the tetracritical point agrees with the previous discussion based on the BEG model, for which the phase diagram with a TCP can be complicated by the presence of bicritical or tetracritical points [43]. Thus, the critical behavior of $\text{Sn}_2\text{P}_2\text{S}_6$ crystals near temperature T_0 requires special attention.

According to previous investigations of thermal diffusivity [58], which is proportional to the reciprocal of heat capacity, the critical behavior of $\text{Sn}_2\text{P}_2\text{S}_6$ crystal can't be self-consistently described in both paraelectric and ferroelectric phases within the framework of appropriate universality class. Such asymmetry is very strange, especially when it has been possible to describe the critical behavior of mixed crystals based on $\text{Sn}_2\text{P}_2\text{S}_6$ using a single model for both phases. For $\text{Sn}_2\text{P}_2(\text{Se}_x\text{S}_{1-x})_6$ solutions with increasing selenium concentration and approaching the LP ($x \approx 0.28$), the critical anomalies are nicely described by exponents and ratios of critical amplitudes that belong to the Lifshitz universality class [see Fig. 8(a)] [59]. When substituting tin by lead in $(\text{Pb}_y\text{Sn}_{1-y})_2\text{P}_2\text{S}_6$ mixed crystals, the critical behavior is also satisfactorily described above and below T_0 as

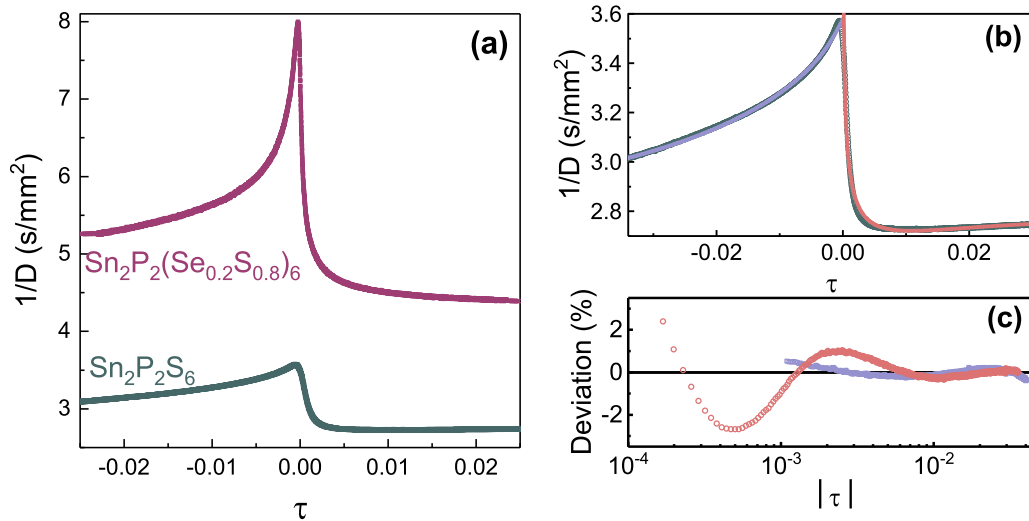


FIG. 8. (a) Dependence of the inverse of thermal diffusivity measured in the [100] crystallographic direction in the vicinity of continuous phase transition in $\text{Sn}_2\text{P}_2\text{S}_6$ and $\text{Sn}_2\text{P}_2(\text{Se}_{0.2}\text{S}_{0.8})_6$ crystals [58,59]. (b) Results of the fittings of the inverse of thermal diffusivity for $\text{Sn}_2\text{P}_2\text{S}_6$ crystal, and (c) corresponding deviation curves for the fittings. The points correspond to experimental measurements, the continuous lines to the fittings to Eq. (6). Blue color corresponds to the fitting below the critical temperature, red to the ones above it.

a crossover from a clear non-mean-field model at $y = 0.1$ to a mean-field one at $y = 0.3$ [36]. For $\text{Sn}_2\text{P}_2\text{Se}_6$ crystals, at the paraelectric to IC second-order phase transition the critical anomaly above and below T_i agrees with the predictions of the renormalization group theory for 3D-XY universality class [61]. When simultaneously substituting different chemical elements in cation and anion sublattices in $(\text{Pb}_y\text{Sn}_{1-y})_2\text{P}_2(\text{Se}_x\text{S}_{1-x})_6$ mixed crystals, a TCLP has been found [56] for $x = 0.28$ and $y = 0.05$ at $T_c = 259.12$ K. Here the tricritical Lifshitz universality class has been assigned because of the obtained critical exponent $\alpha = 0.64$ which is equal to the theoretical predicted one [15].

Why can't a critical behavior of $\text{Sn}_2\text{P}_2\text{S}_6$ crystals be described satisfactorily in both temperature sides of T_0 ? As was mentioned above, for pure $\text{Sn}_2\text{P}_2\text{S}_6$ crystals below T_0 , the coexistence of antipolar (antiferroelectriclike) and ferroelectric states is possible. This is manifested by the observation of double hysteresis loops and usual ferroelectric loops [23]. Considering the possibility of the coexistence of antipolar and ferroelectric phases below T_0 , we reexamine previous experimental data [58]. We have used for the fittings the well-known equation

$$\frac{1}{D} = B + C\tau + A^\pm |\tau|^{-\alpha} (1 + E^\pm |\tau|^{0.5}), \quad (6)$$

where $\tau = (T - T_0)/T_0$ is the reduced temperature and superscripts + and - stand for $T > T_0$ and $T < T_0$, respectively, α , A^\pm , B , C , and E^\pm are adjustable parameters. Figure 8(b) demonstrates the fittings together with the deviation plots [see Fig. 8(c)] (difference between each experimental and fitted value, divided by the experimental value, in percentage).

The results of the fittings [see Fig. 8(b) and 8(c)] in $\text{Sn}_2\text{P}_2\text{S}_6$ have shown an XY-like behavior with the critical exponent $\alpha = -0.0092 \pm 0.0008$ below T_0 and an Ising-like one with $\alpha = 0.1049 \pm 0.0066$ above T_0 . Such value of the critical exponents, smaller than α_{ISING} in the paraelectric phase and a little bigger than α_{XY} below T_0 , can be interpreted

as a possible crossover in the critical behavior which was earlier predicted [72] for systems with two competing order parameters near a bicritical point on the phase diagram. The bicritical point can be originated instead of a tetracritical point if there is a strong enough coupling of two order parameters [73].

In any case, good fittings of thermal diffusivity in a $\text{Sn}_2\text{P}_2\text{S}_6$ crystal below T_0 with negative value of critical index demonstrate that its cups shape is a characteristic of the antiferroelectriclike ordering and coincides with the observed double hysteresis loops in a $\text{Sn}_2\text{P}_2\text{S}_6$ crystal below T_0 [23].

IV. CONCLUSIONS

Static and dynamic critical behavior of $\text{Sn}_2\text{P}_2\text{S}_6$ -type ferroelectrics and $(\text{Pb}_y\text{Sn}_{1-y})_2\text{P}_2(\text{Se}_x\text{S}_{1-x})_6$ mixed crystals are governed by the presence of multicritical points on their phase diagram. Through hydrostatic compression on $\text{Sn}_2\text{P}_2\text{S}_6$ crystal or tin by lead substitution in $(\text{Pb}_y\text{Sn}_{1-y})_2\text{P}_2\text{S}_6$ mixed crystals, the TCP can be reached, which is described by the BC model for a system with three-well local potential for ferroelectric distortion. When replacing sulfur by selenium in $\text{Sn}_2\text{P}_2(\text{Se}_x\text{S}_{1-x})_6$ solid solutions, the LP is induced, which is explained by the first- and second-neighbor short-range interaction ratio changing in the pseudospin ANNNI model. When simultaneously varying the chemical composition in cationic and anionic sublattices, the lines of TCPs and LPs on the $T - x - y$ phase diagram meet at the TCLP, and this higher order multicritical point can be described in a combined BC-ANNNI model—spin-1 Ising model with competing first- and second-neighbor interactions [40,52]. Below the temperature of TCLP, which can be considered the Lifshitz line end point, the chaotic state with coexisting ferroelectric and metastable paraelectric and modulated phases is possible. This expectation agrees with the concentration evolution of heat capacity [63] and dielectric susceptibility [64] temperature dependence in $(\text{Pb}_y\text{Sn}_{1-y})_2\text{P}_2\text{Se}_6$ mixed crystals, which

demonstrates a gradual lock-in transition smearing with the growth of lead concentration.

In addition to the frustration of polar fluctuations near the center of the Brillouin zone, in $\text{Sn}_2\text{P}_2\text{S}_6$ crystals the antipolar fluctuations also strongly develop in the paraelectric phase on cooling to the continuous phase-transition temperature T_0 . This is confirmed by the observation in neutron scattering experiments [46] of a flat polar soft optical phonon branch and by the development of diffuse x-ray scattering along q_y direction in the Brillouin zone of the paraelectric phase near temperature T_0 [51]. Such observation indicates the closeness of this transition to a tetracritical point which appears due to the interaction between two order parameters related to polar fluctuation near the Brillouin zone center and to antipolar fluc-

tuations near its edge. With a strong enough coupling of the mentioned order parameters, the tetracritical point can evolve to a bicritical point. The frequency dependence of the dielectric susceptibility temperature anomaly around T_0 [68,69], together with observed aging effects [74] and transformation of double hysteresis loops into usual ferroelectriclike loops [23] confirm the possibility of simultaneous development of polar and antipolar fluctuations in the paraelectric phase on cooling to T_0 , and the coexistence of antipolar and polar clusters in $\text{Sn}_2\text{P}_2\text{S}_6$ crystals below T_0 . In this transition, the critical behavior according to the thermal diffusivity data [58] can be described as a crossover between Ising and XY universality classes, which is expected near a bicritical point with coupled polar and antipolar order parameters.

-
- [1] A. D. Bruce and R. A. Cowley, *Structural Phase Transitions* (Taylor and Francis Ltd., London, 1981).
- [2] M. E. Lines and A. M. Glass, *Principles and Application of Ferroelectrics and Related Materials* (Clarendon Press, Oxford, 1977).
- [3] R. Blinc and B. Zeks, *Soft Modes in Ferroelectrics and Antiferroelectrics* (North-Holland, Amsterdam, 1974).
- [4] A. Y. Borisevich, E. A. Eliseev, A. N. Morozovska, C.-J. Cheng, J.-Y. Lin, Y. H. Chu, D. Kan, I. Takeuchi, V. Nagarajan, and S. V. Kalinin, *Nat. Commun.* **3**, 775 (2012).
- [5] E. V. Balashova and A. K. Tagantsev, *Phys. Rev. B* **48**, 9979 (1993).
- [6] A. K. Tagantsev, K. Vaideeswaran, S. B. Vakhrushev, A. V. Filimonov, R. G. Burkovsky, A. Shaganov, D. Andronikova, A. I. Rudskoy, A. Q. R. Baron, H. Uchiyama, D. Chernyshov, A. Bosak, Z. Ujma, K. Roleder, A. Majchrowski, J.-H. Ko, and N. Setter, *Nat. Commun.* **4**, 2229 (2013).
- [7] J. Hlinka, T. Ostapchuk, E. Buixaderas, C. Kadlec, P. Kuzel, I. Gregora, J. Kroupa, M. Savinov, A. Klic, J. Drahoukupil, I. Etxebarria, and J. Dec, *Phys. Rev. Lett.* **112**, 197601 (2014).
- [8] R. E. Cohen, *Nature* **358**, 136 (1992).
- [9] W. Zhong and D. Vanderbilt, *Phys. Rev. Lett.* **74**, 2587 (1995).
- [10] W. Zhong, D. Vanderbilt, and K. M. Rabe, *Phys. Rev. B* **52**, 6301 (1995).
- [11] I. Grinberg, V. R. Cooper, and A. M. Rappe, *Nature* **419**, 909 (2002).
- [12] L. Bellaiche, A. Garcia, and D. Vanderbilt, *Phys. Rev. Lett.* **84**, 5427 (2000).
- [13] N. Sai and D. Vanderbilt, *Phys. Rev. B* **62**, 13942 (2000).
- [14] R. Folk and G. Moser, *Phys. Rev. B* **47**, 13992 (1993).
- [15] R. Folk, *Phase Transit.* **67**, 645 (1999).
- [16] Yu. M. Vysochanskii, M. M. Mayor, V. M. Rizak, V. Yu. Slivka, and M. M. Khoma, *JETP* **68**, 782 (1989).
- [17] Yu. M. Vysochanskii and V. Yu. Slivka, *Sov. Phys. Usp.* **35**, 123 (1992).
- [18] A. A. Grabar, Y. M. Vysochanskii, A. N. Shumelyuk, M. Jazbinsek, G. Montemezzani, and P. Gunter, in *Photorefractive Materials and Their Applications*, edited by P. Gunter and J. P. Huignard (Springer Verlag, Heidelberg, 2006).
- [19] Y. W. Cho, S. K. Choi, and Yu. M. Vysochanskii, *J. Mater. Res.* **16**, 3317 (2001).
- [20] S. Huang, C. Meng, M. Xiao, S. Ren, Sh. Wang, D. Han, Yu. Li, and Yu. Meng, *Small* **14**, 1704367 (2018).
- [21] F. C. Penning, M. M. Maior, S. A. J. Wieggers, H. van Kempen, and J. C. Maan, *Rev. Sci. Instrum.* **67**, 2602 (1996).
- [22] M. M. Major, Sh. B. Molnar, Yu. M. Vysochanskii, M. I. Gurzan, P. H. M. van Loosdrecht, P. J. E. M. van der Linden, and H. van Kempen, *Appl. Phys. Lett.* **62**, 2646 (1993).
- [23] I. Zamaraitė, R. Yevych, A. Dziaugys, A. Molnar, J. Banys, S. Svirskas, and Yu. Vysochanskii, *Phys. Rev. Appl.* **10**, 034017 (2018).
- [24] S. Grubel, J. A. Johnson, P. Beaud, C. Dornes, A. Ferrer, V. Haborets, L. Huber, T. Huber, A. Kohutych, T. Kubacka, M. Kubli, S. O. Mariager, J. Rittmann, J. I. Saari, Y. Vysochanskii, G. Ingold, and S. L. Johnson, *arXiv:1602.05435*.
- [25] E. A. Eliseev, Y. M. Fomichov, S. V. Kalinin, Yu. M. Vysochanskii, P. Maksymovich, and A. N. Morozovska, *Phys. Rev. B* **98**, 054101 (2018).
- [26] A. N. Morozovska, Eu. A. Eliseev, Y. M. Fomichov, Yu. M. Vysochanskii, V. Yu. Reshetnyak, and D. R. Evans, *Acta Mater.* **183**, 36 (2020).
- [27] G. Dittmar and H. Schafer, *Z. Naturforsch B* **29**, 312 (1974); B. Scott, M. Pressprich, R. D. Willet, and D. A. Cleary, *J. Solid State Chem.* **96**, 294 (1992).
- [28] K. Z. Rushchanskii, Yu. M. Vysochanskii, and D. Strauch, *Phys. Rev. Lett.* **99**, 207601 (2007).
- [29] A. N. Rubtsov, J. Hlinka, and T. Janssen, *Phys. Rev. E* **61**, 126 (2000).
- [30] J. Hlinka, T. Janssen, and V. Dvořák, *J. Phys.: Condens. Matter* **11**, 3209 (1999).
- [31] K. Moriya, H. Kuniyoshi, K. Tashita, Y. Ozaki, S. Yano, and T. Matsuo, *J. Phys. Soc. Jpn.* **67**, 3505 (1998).
- [32] Yu. M. Vysochanskii, T. Janssen, R. Currat, R. Folk, J. Banys, J. Grigas, and V. Samulionis, *Phase Transitions in Ferroelectric Phosphorous Chalcogenide Crystals* (Vilnius University Publishing House, Vilnius, 2006).
- [33] P. Ondrejko, M. Kempa, Y. Vysochanskii, P. Saint-Gregoire, P. Bourges, K. Z. Rushchanskii, and J. Hlinka, *Phys. Rev. B* **86**, 224106 (2012).
- [34] P. Ondrejko, M. Guennou, M. Kempa, Y. Vysochanskii, G. Garbarino, and J. Hlinka, *J. Phys.: Condens. Matter* **25**, 115901 (2013).

- [35] K. Z. Rushchanskii, R. M. Bilanych, A. A. Molnar, R. M. Yevych, A. A. Kohutych, S. I. Perechinskii, V. Samulionis, J. Banys, and Y. M. Vysochanskii, *Phys. Status Solidi B* **253**, 384 (2016).
- [36] V. Shvalya, A. Oleaga, A. Salazar, A. A. Kohutych, and Yu. M. Vysochanskii, *Thermochim. Acta* **617**, 136 (2015).
- [37] R. Yevych, V. Haborets, M. Medulych, A. Molnar, A. Kohutych, A. Dziaugys, Ju. Banys, and Yu. Vysochanskii, *Low Temp. Phys.* **42**, 1155 (2016).
- [38] X. Bourdon, A. Grimmer, A. Kretschmer, and V. Cajipe, in *Proceedings of the 30th Congress Ampere on Magnetic Resonance and Related Phenomena* (NOVA University Lisbon, Portugal, 2000).
- [39] K. Glukhov, K. Fedyo, J. Banys, and Yu. Vysochanskii, *Int. J. Mol. Sci.* **13**, 14356 (2012).
- [40] T. Tome and S. R. Salinas, *Phys. Rev. A* **39**, 2206 (1989).
- [41] M. Blume, *Phys. Rev.* **141**, 517 (1966); H. W. Capel, *Physica* **32**, 966 (1966).
- [42] M. Blume, V. J. Emery, and R. B. Griffiths, *Phys. Rev. A*, **4**, 1071 (1971).
- [43] W. Hoston and A. N. Berker, *Phys. Rev. Lett.* **67**, 1027 (1991).
- [44] W. Selke, *Phys. Rep.* **170**, 213 (1988).
- [45] S. W. H. Eijt, R. Currat, J. E. Lorenzo, P. Saint-Grégoire, S. Katano, T. Janssen, B. Hennion, and Yu. M. Vysochanskii, *J. Phys.: Cond. Matt.* **10**, 4811 (1998).
- [46] S. W. H. Eijt, R. Currat, J. E. Lorenzo, P. Saint-Grégoire, B. Hennion, and Yu. M. Vysochanskii, *Eur. Phys. J. B* **5**, 169 (1998).
- [47] A. Kohutych, R. Yevych, S. Perechinskii, V. Samulionis, J. Banys, and Yu. Vysochanskii, *Phys. Rev. B* **82**, 054101 (2010).
- [48] A. N. Morozovska, Yu. M. Vysochanskii, O. V. Varenyk, M. V. Silibin, S. V. Kalinin, and Eu. A. Eliseev, *Phys. Rev. B* **92**, 094308 (2015).
- [49] A. N. Morozovska, M. D. Glinchuk, E. A. Eliseev, and Yu. M. Vysochanskii, *Phys. Rev. B* **96**, 094111 (2017).
- [50] R. M. Yevych, Yu. M. Vysochanskii, M. M. Khoma, and S. I. Perechinskii, *J. Phys.: Condens. Matter* **18**, 4047 (2006).
- [51] J. Hlinka, R. Currat, M. de Boissieu, F. Livet, and Yu. M. Vysochanskii, *Phys. Rev. B* **71**, 052102 (2005).
- [52] P. J. Jensen, K. A. Penson, and K. H. Bennemann, *Phys. Rev. B* **35**, 7306 (1987).
- [53] A. Aharony, E. Domany, R. M. Hornreich, T. Schneider, and M. Zannetti, *Phys. Rev. B* **32**, 3358 (1985).
- [54] N. S. Tonchev and D. I. Uzunov, *Physica A* **134**, 265 (1985).
- [55] Afaf Abdel-Hady and R. Folk, *Phys. Rev. B* **54**, 3851 (1996).
- [56] A. Oleaga, V. Shvalya, A. Salazar, I. Stoika, and Yu. M. Vysochanskii, *J. Alloys Compd.* **694**, 808 (2017).
- [57] T. M. Rice and L. Sneddon, *Phys. Rev. Lett.* **47**, 689 (1981).
- [58] A. Oleaga, A. Salazar, M. Massot, and Yu. M. Vysochanskii, *Thermochim. Acta* **459**, 73 (2007).
- [59] A. Oleaga, A. Salazar, A. A. Kohutych, Yu. M. Vysochanskii, *J. Phys.: Condens. Matter* **23**, 025902 (2011).
- [60] V. Shvalya, A. Oleaga, A. Salazar, I. Stoika, and Yu. M. Vysochanskii, *J. Mater. Sci.* **51**, 8156 (2016).
- [61] V. Shvalya, A. Oleaga, A. Salazar, A. A. Kohutych, and Yu. M. Vysochanskii, *J. Phys. Chem. Solids* **88**, 78 (2016).
- [62] A. Oleaga, V. Liubachko, A. Salazar, and Yu. Vysochanskii, *Thermochim. Acta* **675**, 38 (2019).
- [63] K. Moriya, T. Yamada, K. Saka, S. Yano, S. Baluya, T. Matsuo, P. Pritz, and Yu. Vysochanskii, *J. Therm. Anal. Calorim.* **70**, 321 (2002).
- [64] Yu. M. Vysochanskii, M. M. Maior, V. Yu. Slivka, and M. I. Gurzan, *Fiz. Tverd. Tela* **27**, 1560 (1985) [in Russian].
- [65] V. Yu. Korda, S. V. Berezovsky, A. S. Molev, L. P. Korda, and V. F. Klepikov, *Physica B* **407**, 3388 (2012).
- [66] V. Yu. Korda, S. V. Berezovsky, A. S. Molev, L. P. Korda, and V. F. Klepikov, *Physica B* **425**, 31 (2013).
- [67] G. H. F. van Raaij, K. J. H. van Bommel, and T. Janssen, *Phys. Rev. B* **62**, 3751 (2000).
- [68] A. A. Volkov, G. V. Kozlov, N. I. Afanasjeva, A. A. Grabar, Yu. M. Vysochanskii, and V. Yu. Slivka, *Fiz. Tverd. Tela* **25**, 2575 (1983) [in Russian].
- [69] J. Grigas, *Ferroelectrics* **380**, 113 (2009).
- [70] R. Yevych, M. Medulych, and Yu. Vysochanskii, *Condens. Matter Phys.* **21**, 23001 (2018).
- [71] R. Yevych and Yu. Vysochanskii, *Condens. Matter Phys.* **21**, 33001 (2018).
- [72] J. M. Kosterlitz, D. R. Nelson, and M. E. Fishert, *Phys. Rev. B* **13**, 412 (1976).
- [73] R. Folk, Yu. Holovatch, and G. Moser, *Phys. Rev. E* **78**, 041124 (2008).
- [74] A. A. Molnar, Yu. M. Vysochanskii, A. A. Gorvat, and Yu. S. Nakonechnii, *Ferroelectrics* **174**, 41 (1995).